Chapter 4

4. MODIFIED SBA-15 SUPPORTED ZnO AND SnO_2 NANOCATALYSTS FOR FRIEDEL-CRAFTS ACYLATION OF ANISOLE WITH BENZOIC ANHYDRIDE

This chapter presents the complete characterization and application of ZnO and SnO_2 supported on mesoporous silica SBA-15 modified by using a swelling agent, trimethylbenzene. The catalytic activity of the synthesized catalysts is further evaluated for the Friedel-Crafts acylation of anisole with benzoic anhydride. The synthetic procedures for the catalysts and their characterization techniques are described in Chapter 2.

4.1 Prologue

Friedel-Crafts (FC) acylation reaction is ubiquitous in various industries for the synthesis of aromatic ketones [1–3]. The FC acylation of anisole is an industrially important reaction and the ketone produced thereof can also be further hydrogenated to commercially useful secondary alcohol [4]. The traditionally used acylating agents are generally acid halides that undergo electrophilic substitution reactions with aromatic rings to produce aromatic ketones [5]. However, these expensive and harmful acid halides necessitate special care during handling and workup [6]. Moreover, the use of acid halides results in the generation of halogen acids as by-products which results in reactor corrosion and environmental pollution [7]. In this context, relatively cheap, readily available, and non-polluting carboxylic acids and anhydrides are scoped as beneficial alternatives to halogenated agents when more effective acid catalysts are available [8]. There are a few publications in the literature that have reported the utilization of benzoic anhydride to acylate anisole [7, 9–13].

The conventionally used catalysts (anhyd. $AlCl_3$, $FeCl_3$, H_2SO_4 etc.) for FC acylation, as discussed earlier in Chapters 1 and 3, are associated with drawbacks that include difficulty in handling and recovery due to their highly reactive and moisture-sensitive nature. To overcome these drawbacks, heterogeneous solid acids such as zeolites, clays, heteropoly acids, metal oxides, etc. are increasingly preferred as catalysts for FC acylation owing to their non-corrosive and non-toxic nature, reusability, and easy separation [14]. Among the solid acids, nanoscale metal oxides have garnered special interest due to their improved reactivity and selectivity [15, 16]. However, the bare metal oxide nanocatalysts often suffer leaching and agglomeration during the reaction and

possess moderate Lewis acidity [17]. To address these issues, the metal oxide phase is generally dispersed onto a suitable large surface area support [11]. Microporous supports such as zeolites are less favourable as catalyst supports due to mass transfer limitations that are related to their microporous system [18]. Mesoporous silica materials such as MCM-41, SBA-15, etc. are promising candidates for support due to their tunable pore size, high surface area, and thermal stability [19]. Particularly, SBA-15 possesses a robust matrix for incorporating nanoparticles due to its thicker walls and relatively larger pore size. Immobilization of the active phase, i.e., metal oxide within the silica matrix prevents its agglomeration and surface fouling as well as aids its recovery [20]. The pore size of SBA-15 is adjustable in the range 5–30 nm depending on the synthesis route which assists in accommodating bulky reactants and products during a reaction [21]. Hence, in this chapter, SBA-15 is modified by using a swelling agent, trimethylbenzene, and utilized as a support material for ZnO and SnO_2 nanoparticles. The synthesized supported nanocatalysts are further employed for the FC acylation of anisole with benzoic anhydride.

4.2 Results and discussion

4.2.1 Characterization

Figure 4.1a displays the FTIR spectra of the synthesized samples: modified SBA-15, ZS, and TS. All the spectra depict a broad band at 3445 cm^{-1} corresponding to O–H stretching vibrations of adsorbed H_2O and surface Si–OH bonds of silanol groups [22]. The in-plane H–O–H bending vibrations occurring at 1630 cm^{-1} confirm the presence of

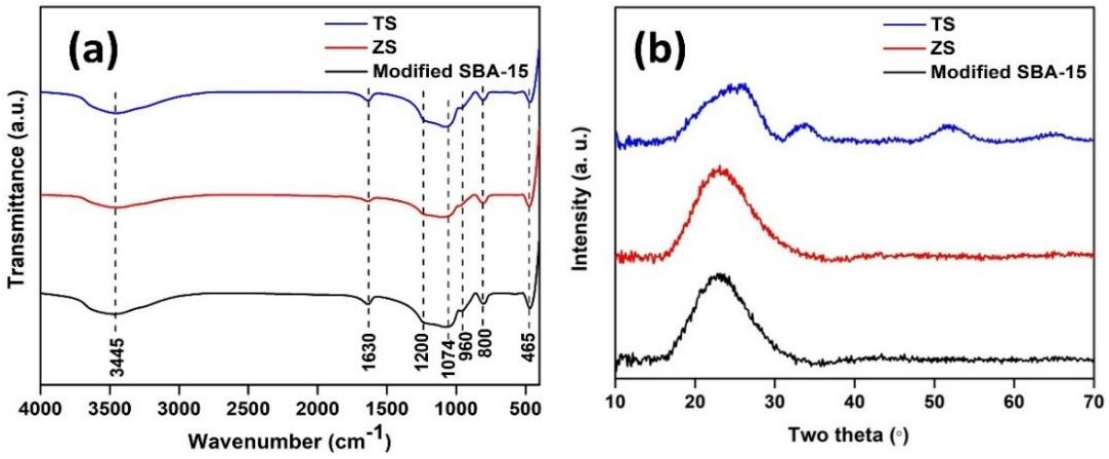

Figure 4.1 FTIR (a) and XRD (b) patterns of synthesized samples: modified SBA-15, ZS, and TS.

adsorbed water. The weak band at 960 cm^{-1} corresponds to stretching vibrations of Si–OH groups. This band is considerably attenuated in the ZS and TS samples, implying interactions between the silica host and the metal oxide phase. Again, the bands at 1200-1074 and 800 cm^{-1} are attributable to the asymmetric and symmetric stretching vibrations of Si–O–Si bonds, respectively [18]. The band at 465 cm^{-1} corresponds to O–Si–O bending vibrations of the samples. The appearance of these bands implies that the silanol and siloxane groups forming the modified SBA-15 framework are stable after the incorporation of the metal oxides.

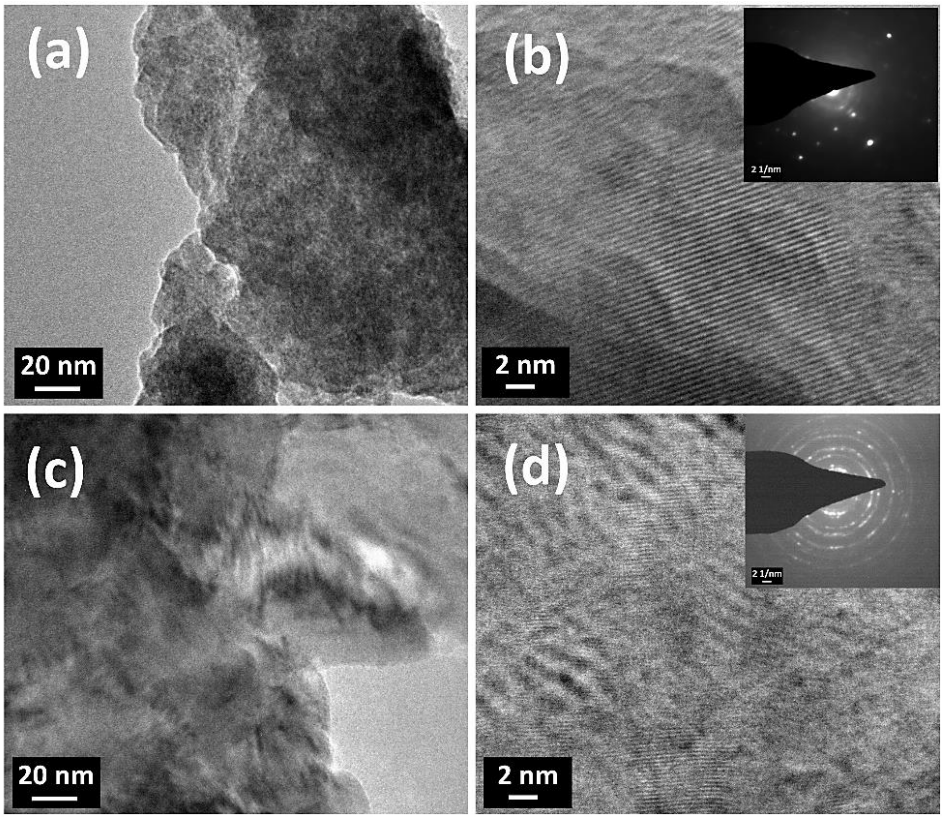

Figure 4.2 TEM and HRTEM images of ZS (a, b) and TS (c, d); insets in c and d show SAED pattern of the corresponding samples.

Figure 4.1b represents the XRD patterns of the synthesized samples. All the samples show a broad peak at $2\theta = 23°$ which is indicative of amorphous SiO_2 [18]. The XRD pattern of TS contains peaks corresponding to both amorphous walls of mesoporous silica and tetragonal SnO_2 phase in accordance with JCPDS Card No. 01-070-6153 [23]. However, no diffraction peaks corresponding to ZnO phase are observed in ZS which indicates that this phase is dispersed well into the silica support as nanocrystals with sizes beyond the detection limit of XRD [18].

Figure 4.2 illustrates the TEM analysis of ZS and TS samples. The TEM and HRTEM images of ZS (Figures 4.2a and b) and TS (Figures 4.2c and d) demonstrate numerous dark areas that reflect the existence of metal oxide nanoparticles which are distributed in the mesopores of the modified SBA-15 support. The SAED pattern of ZS sample (inset in Figure 4.2b) exhibits bright spotty pattern suggesting single crystalline nature of the sample [24]. Again, the SAED pattern of TS (inset in Figure 4.2d) exhibits well resolved rings indicating a polycrystalline nature [25].

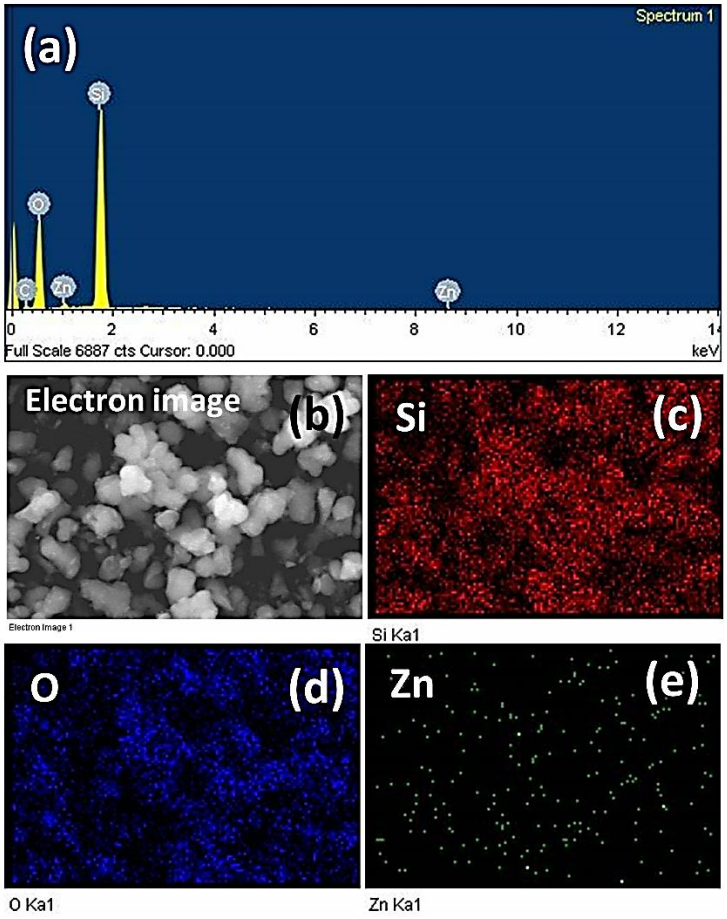

Figure 4.3 EDX pattern (a), electron image (b), and EDS mapping of Si (c), O (d) & Zn (e) of ZS sample.

EDS analysis in combination with elemental mapping is performed to evaluate the existence and dispersion of metal oxide phases in the modified SBA-15 support [26**]**. The EDS analysis of ZS shown in Figure 4.3a affirms the presence of Si, O, and Zn in the synthesized sample. Moreover, the EDS elemental mappings of the selected area in Figure 4.3b display the uniform dispersion of Zn over the silica support in the ZS sample. The content of Zn obtained from EDS analysis is approximately 0.49 at.%, verifying that a small amount of ZnO is loaded on the mesoporous silica support [27]. Again, the EDS

analysis of TS displayed in Figure 4.4a confirms the presence of Si, O, and Sn in the material. EDS mappings of the selected area in Figure 4.4b shows that Sn is distributed uniformly in the silica support, and the content of Sn is ~0.89 at.%.

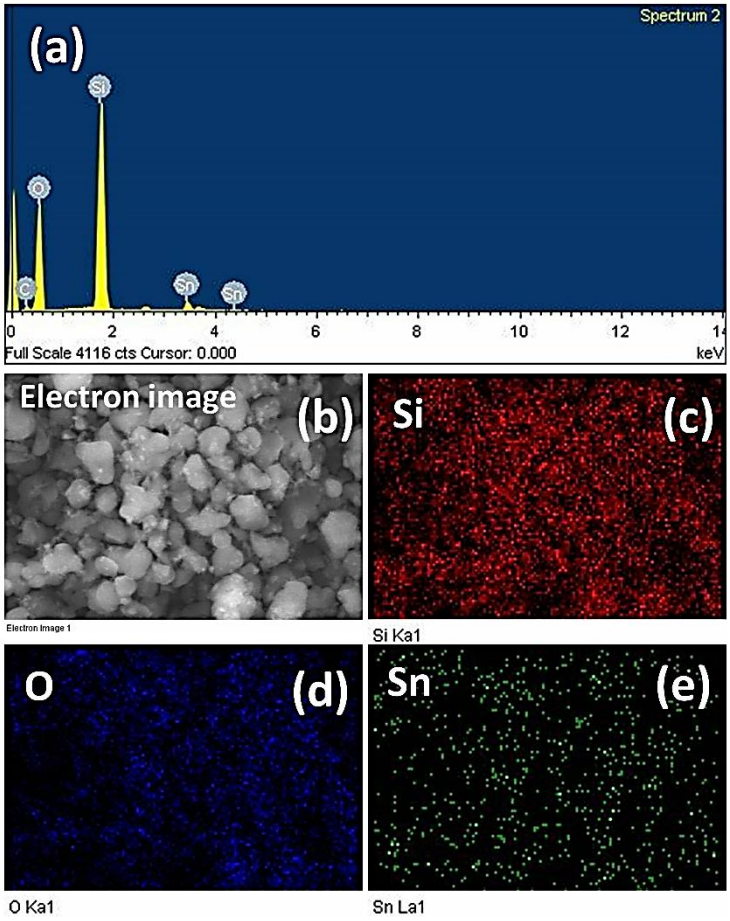

Figure 4.4 EDX pattern (a), electron image (b), and EDS mapping of Si (c), O (d) & Zn (e) of TS sample.

The chemical constituents and valence state of ZS and TS are studied by XPS and the results are presented in Figures 4.5 and 4.6, respectively. The XPS survey spectrum of ZS shown in Figure 4.5a confirms the presence of Si, O, and Zn in the sample. The higher intensities of O and Si are indicative of their greater proportion in the sample [28]. The Si 2p peak at 103.7 eV in the Si 2p XPS spectrum of ZS displayed in Figure 4.5b corresponds to the binding energy of Si 2p (~103.6 eV) associated with standard spectrum of SiO_2 [29]. The high-resolution Zn 2p XPS spectrum of ZS displayed in Figure 4.5c shows two peaks at 1045.9 and 1022.9 eV, attributable to Zn $2p_{3/2}$ and Zn $2p_{1/2}$ with an energy splitting value of 23 eV which agrees well with that of ZnO [30]. Both the peaks of Zn $2p_{3/2}$ and Zn $2p_{1/2}$ shift to higher binding energies compared to reported pure ZnO, suggesting a change in the binding state of Zn ions in the sample that is caused by the formation of Zn−O−Si

cross-linking bonds at the interface between SiO_2 and ZnO [31]. The O1s spectrum in Figure 4.5d is deconvoluted into three Gaussian peaks centered at ~530.6, 532.9, and 533.9 eV that are ascribed to oxygen from Zn−O, Si−O, and O−H, respectively [19, 28].

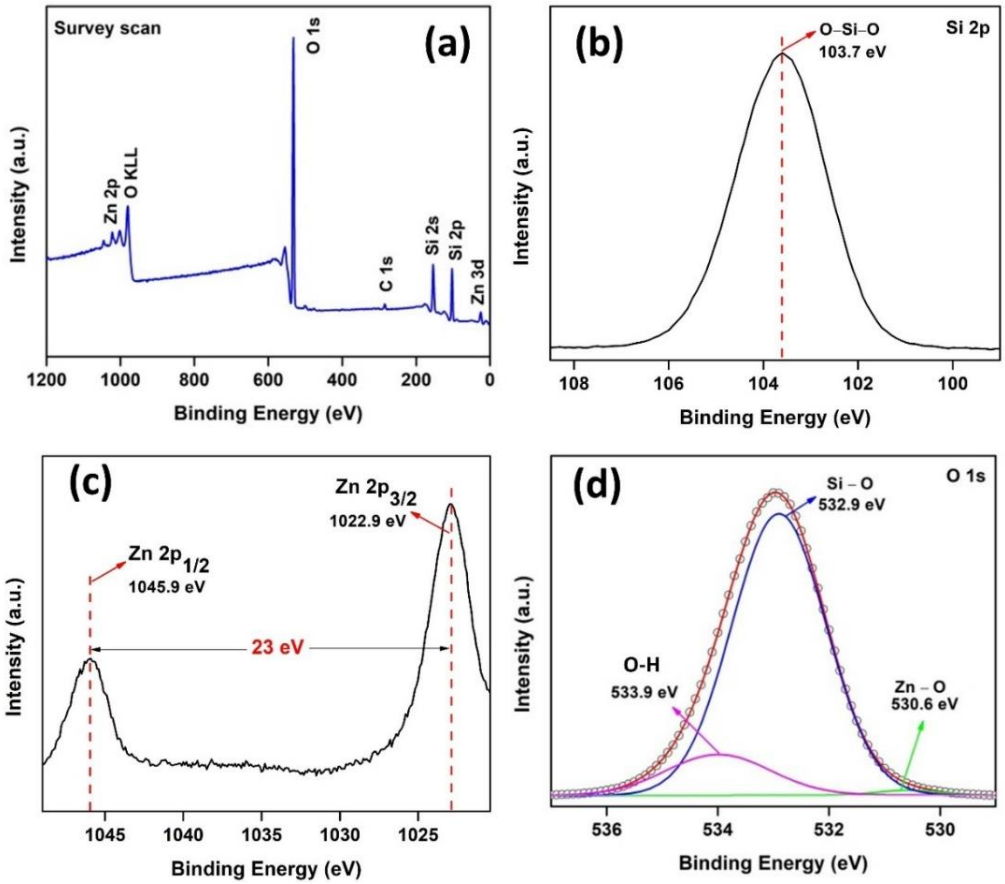

Figure 4.5 EDX pattern (a), electron image (b), and EDS mapping of Si (c), O (d) and Zn (e) of ZS sample.

Again, the XPS survey spectrum of TS shown in Figure 4.6a confirms the presence of the elements Si, O, and Sn in the sample. The Si 2p XPS spectrum of TS in Figure 4.6b shows a peak at 103.7 eV corresponding to the typical Si 2p peak of O−Si−O in SiO_2. Figure 4.6c displays the high-resolution Sn 3d XPS spectrum of TS. The two peaks centered at 487.5 eV and 495.9 eV are attributable to Sn $3d_{5/2}$ and Sn $3d_{3/2}$, respectively with a spin-orbit splitting of 8.4 eV which indicates the existence of Sn^{4+} and formation of SnO_2 [32]. No signals are observed for metallic Sn (493.2 eV and 484.8 eV), demonstrating that Sn is present in the form of oxides in the sample. The deconvoluted O 1s XPS spectrum in Figure 4.6d depicts three Gaussian peaks centered at ~532.2, 532.9, and 533.6 eV corresponding to oxygen from Sn−O, Si−O, and O−H, respectively. The binding energies of the peaks in the O 1s spectrum are slightly changed compared to the

reported values of SnO_2 and SiO_2, implying the existence of interaction between SnO_2 and modified SBA-15 support [28].

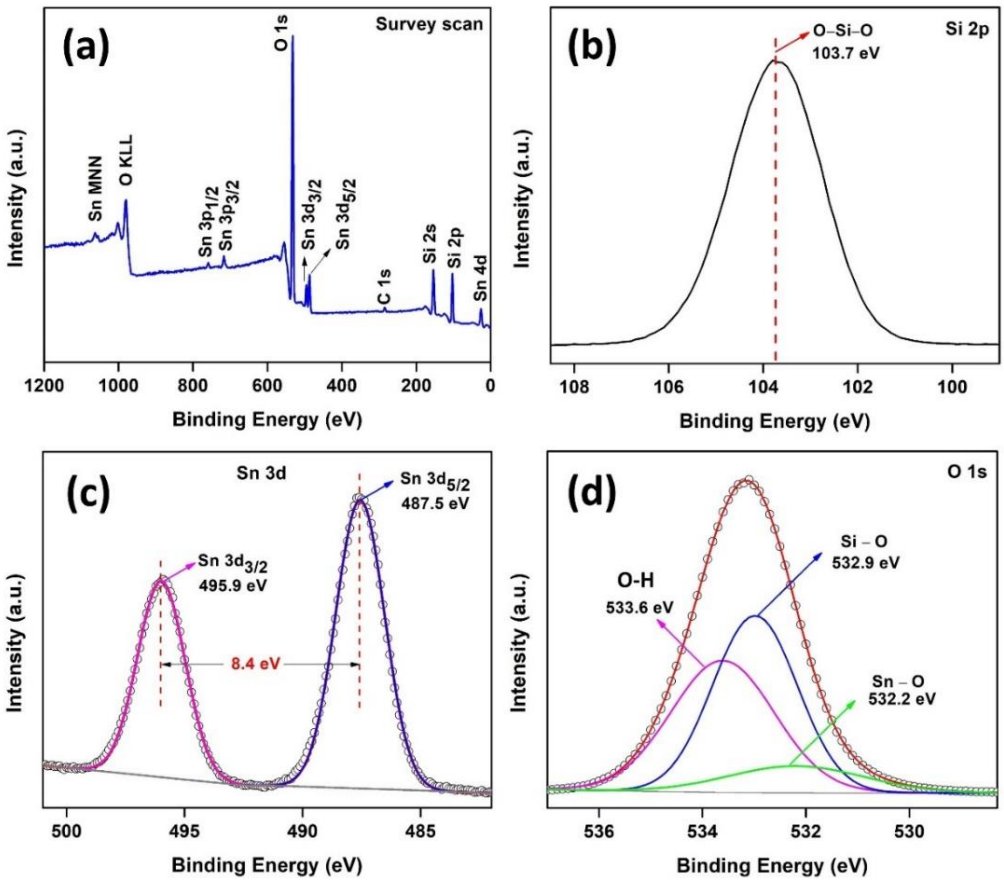

Figure 4.6 EDX pattern (a), electron image (b), and EDS mapping of Si (c), O (d) & Zn (e) of TS sample.

Figure 4.7 depicts the N_2 adsorption-desorption isotherms and the corresponding pore size distribution curves of the synthesized samples. The isotherms of all the samples belong to type IV, indicating that the materials are mesoporous in nature [33].

Table 4.1 depicts a comparison of the surface area and pore structure parameters of the synthesized samples. As shown in Table 4.1, the specific surface area of modified SBA-15 is 673.6 m^2g^{-1}. The pore volume and average pore diameter calculated using the BJH method are 2.40 cm^3g^{-1} and 10.9 nm, respectively. The surface area of the samples upon the incorporation of the metal oxides reduces to 416.9 and 334.7 m^2g^{-1} for ZS and TS, respectively. Similarly, the pore volume and pore diameter of the metal oxide incorporated samples also decrease compared to that of modified SBA-15 silica support. These observations are attributable to the dispersion of the metal oxide particles in the mesoporous silica channels [30].

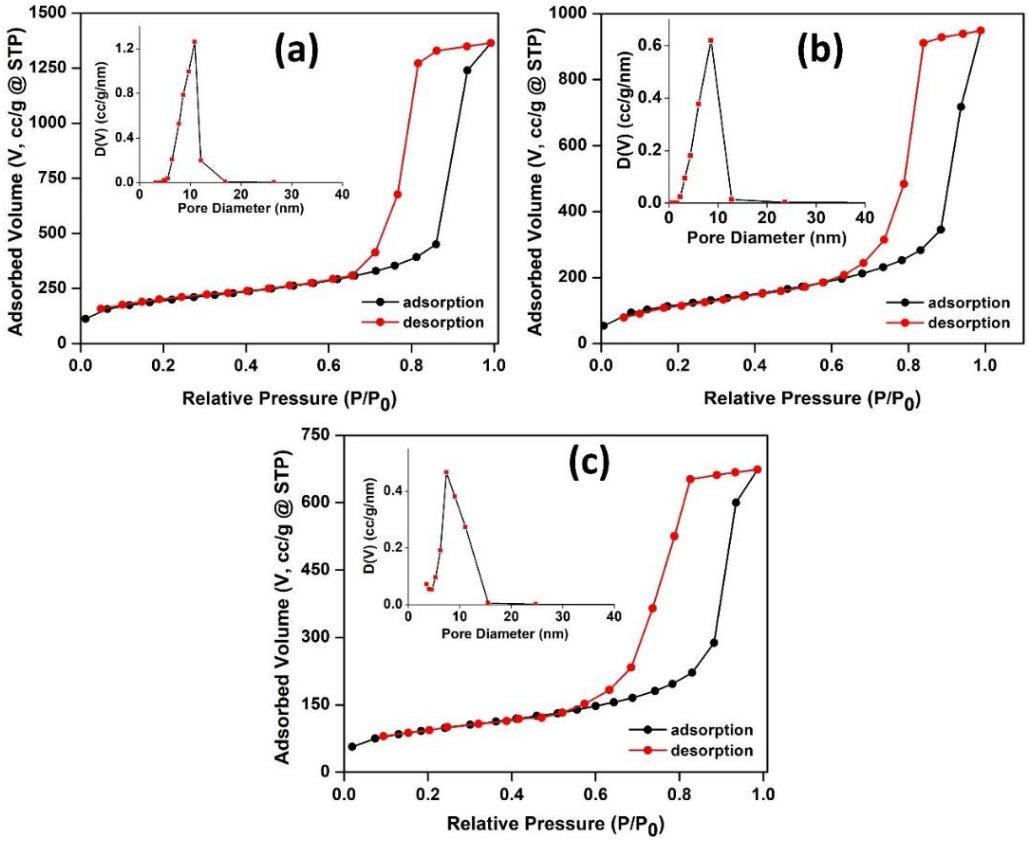

Figure 4.7 N_2 adsorption-desorption isotherms of modified SBA-15 (a), ZS (b), and TS (c); insets (a–c): pore size distribution curve of the respective samples.

Table 4.1 Physical parameters of the synthesized samples obtained from N_2 adsorption-desorption analysis.

Sample	BET surface area m^2g^{-1}	Pore volume cm^3g^{-1}	Average pore diameter (nm)
Modified SBA-15	673.6	2.40	10.9
ZS	416.9	1.59	8.6
TS	334.7	1.20	7.4

The acidic properties of the ZS and TS samples are evaluated using Hammett indicator-amine titration method. The acidic strength and amount of acid sites of the synthesized samples are presented in Table 4.2. The acid strength of both the samples lies in the range of 4.8–3.4. The amount of acid sites determined using amine titration is found to be 1.5 and 2.4 mmol g^{-1} for ZS and TS, respectively. The higher amount of acid sites in TS compared to ZS could be ascribable to the better loading of SnO_2 into the silica support as evidenced by EDX analysis.

Table 4.2 Acidic properties of ZS and TS samples.

Sample	Acid strength range	Amount of acid sites (mmol g^{-1})
Modified SBA-15	4.8–3.4	0.5
ZS	4.8–3.4	1.5
TS	4.8–3.4	2.4

4.2.2 Catalytic activity

The catalytic activities of the ZnO and SnO_2 supported on modified SBA-15 are evaluated for the Friedel-Crafts acylation of anisole with benzoic anhydride. Both the catalysts afford acceptable yields with high regioselectivity in the para position (Table 4.3, entries 1 and 2) and generate benzoic acid as the by-product. The activity of the TS catalyst for this reaction is superior to that of ZS, which could be attributed to better loading and higher acidity. It should be noted herein that the acylation is also carried out using benzoic acid as an acylating agent (Table 4.3, entry 3). However, no reaction is observed with benzoic acid using TS as catalyst under similar reaction conditions. This observation confirms that there is no role of benzoic acid which is formed as by-product during the acylation reaction of anisole with benzoic anhydride. A blank experiment conducted without the catalyst did not result in the conversion of benzoic anhydride, implying the role of the catalyst (Table 4.3, entry 4).

Table 4.3 Results of FC acylation of anisole with different catalysts and acylating agents.[a]

Entry	Acylating agent	Catalyst	Yield[b]
1	Benzoic anhydride	ZS	46
2	Benzoic anhydride	TS	65
3	Benzoic acid	TS	n.r
4	Benzoic anhydride	None	n.r

[a]Reaction conditions: *n*(anisole):*n*(benzoic anhydride) = 1:2, catalyst dosage (0.03 g), temperature (100 °C), and time (10 h).

[b]Isolated yield.

n.r: no reaction.

4.2.2.1 Optimization study

All the experiments are carried out using TS as the catalyst considering its better catalytic activity than ZS. The effects of various parameters such as catalyst dosage,

temperature, solvent, and molar ratio of reactants on the acylation reaction are investigated and the results are presented in Table 4.4.

4.2.2.1a Effect of catalyst dosage

The effect of catalyst dosage on the acylation reaction is studied using 0.03, 0.05, and 0.07 g of catalyst as shown in Table 4.4, entries 1–3. The yield of the reaction increases as the catalyst dosage is increased from 0.03 to 0.05 g. This could be substantiated by the proportional increase in catalytically active sites with increasing catalyst dosage. However, no significant improvement in the yield of the reaction is achieved beyond 0.05 g which could be due to the occurrence of deep reaction and resistance in mass transfer with an excessive amount of catalyst [34]. Hence, 0.05 g is chosen as the optimum amount of catalyst for the reaction.

Table 4.4 Optimization of reaction parameters for the FC acylation of anisole with benzoic anhydride using TS.[a]

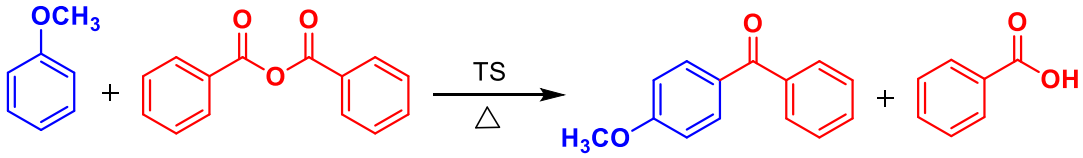

Entry	Catalyst dosage (g)	Temperature (°C)	Solvent	Substrate ratio	Isolated yield (%)
1	0.03	100	CH_3NO_2	1:2	65
2	0.05	100	CH_3NO_2	1:2	72
3	0.07	100	CH_3NO_2	1:2	70
4	0.05	60	CH_3NO_2	1:2	35
5	0.05	80	CH_3NO_2	1:2	48
6	0.05	120	CH_3NO_2	1:2	69
7	0.05	100	CH_3CN	1:2	45
8	0.05	100	CH_2Cl_2	1:2	50
9	0.05	100	THF	1:2	30
10	0.05	100	None	1:2	55
11	0.05	100	CH_3NO_2	2:1	57
12	0.05	100	CH_3NO_2	1:1	35

[a]Reaction conditions: solvent = 0.5 mL and time = 10 h.

4.2.2.1b Effect of temperature

The variation in catalytic activity at different temperatures from 60 to 120 °C is explored and the results are presented in Table 4.4, entries 2, 4–6. As observed, the catalytic activity improves with the increase in temperature up to 100 °C which may be attributed to the enhanced molecular collision and miscibility of the reactants [34]. The yield of reaction did not change much upon increasing the temperature to 120 °C. Therefore, further studies are conducted at 100 °C with a catalyst dosage of 0.05 g.

4.2.2.1c Effect of solvent

The effect of various solvents such as nitromethane (CH_3NO_2), acetonitrile (CH_3CN), dichloromethane (CH_2Cl_2), and tetrahydrofuran (THF) on the catalytic activity is presented in Table 4.4, entries 2, 7–10. As evident from the results, the best yield (72%) of 4-methoxybenzophenone is obtained using CH_3NO_2 as the solvent probably due to its high polarity and weakly coordinating nature [35]. Therefore, CH_3NO_2 is chosen as the best solvent for the acylation reaction.

4.2.2.1d Effect of molar ratio of substrates

The effect of molar ratio of anisole to benzoic anhydride (*n*(anisole):*n*(benzoic anhydride)) on the acylation is studied by keeping all other variables constant (Table 4.4, entries 2, 10 and 11). Increasing the number of moles of benzoic anhydride with respect to anisole results in higher yield of 4-methoxybenzophenone. This observation could be attributed to the higher concentration of electrophile generated from benzoic anhydride to react with nucleophilic anisole [36]. However, a further increase in the number of moles of benzoic anhydride might result in the dilution of anisole, thereby inhibiting the effective collision between the reactants [34]. The results suggest that 1:2 molar ratio of anisole to benzoic anhydride is optimum for the acylation reaction.

4.2.2.2 Recyclability test

The recyclability of the synthesized catalyst is studied for the FC acylation of anisole with benzoic anhydride under the optimum reactions. For the recyclability test, the TS catalyst is separated from the reaction mixture by centrifugation and washed with ethanol for several times for the removal of impurities and finally dried overnight at 80 °C. The regenerated catalyst is then dispersed in a fresh reaction mixture for subsequent cycles and the results are presented in Figure 4.8. A marginal loss of about 10% (Figure

4.8a) in the yield of the product is observed after four consecutive cycles, probably due to the loss of catalyst during regeneration. The recovered catalyst is characterized by XRD to determine its structural stability. The XRD pattern of the recovered catalyst displayed in Figure 4.8b shows inconsequential changes compared to the fresh catalyst, suggesting its good structural stability even after reuse.

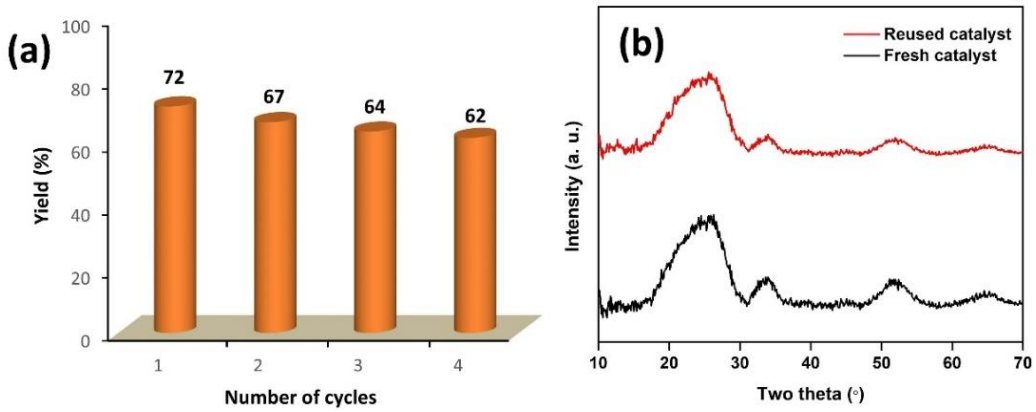

Figure 4.8 Recyclability test (a), XRD patterns of fresh and reused TS catalyst (b).

In summary, we have synthesized ZnO and SnO_2 supported on SBA-15 modified by using trimethylbenzene as swelling agent. The structural, morphological, and compositional analyses of the synthesized samples reveal the successful incorporation of the metal oxides into the mesoporous channels and surfaces of the silica support. The synthesized catalysts are further employed for the FC acylation of anisole with benzoic anhydride. Both the synthesized catalysts could furnish acceptable yields of 4-methoxybenzophenone as the product. SnO_2 supported on modified SBA-15 shows better catalytic activity compared to that of ZnO which is attributable to its better loading and higher acidity. Furthermore, the catalyst is recycled up to four consecutive cycles with minimal loss of catalytic activity.

REFERENCES

[1] Martins, A., Neves, V., Moutinho, J., Nunes, N., and Carvalho, A. P. Friedel-Crafts acylation reaction over hierarchical Y zeolite modified through surfactant mediated technology. *Microporous and Mesoporous Materials*, 323:111167, 2021.

[2] Yadav, G. D. and Kamble, S. B. Atom efficient Friedel-Crafts acylation of toluene with propionic anhydride over solid mesoporous superacid UDCaT-5. *Applied Catalysis A: General*, 433:265–274, 2012.

[3] Kantam, M. L., Ranganath, K. V. S., Sateesh, M., Kumar, K. B. S., and Choudary, B. M. Friedel-Crafts acylation of aromatics and heteroaromatics by beta zeolite. *Journal of Molecular Catalysis A: Chemical*, 225(1):15–20, 2005.

[4] Lu, H., Xie, J., Wu, X., Ma, Q., Cheng, J., Li, Z., and Hu, D. Highly efficient Friedel-Crafts acylation of veratrole over TiO_2-SnO_x solid solution catalyst. *Applied Catalysis A: General*, 648:118922, 2022.

[5] Zhang, H., Song, X., Hu, D., Zhang, W., and Jia, M. Iron-based nanoparticles embedded in a graphitic layer of carbon architectures as stable heterogeneous Friedel-Crafts acylation catalysts. *Catalysis Science & Technology*, 9(14):3812–3819, 2019.

[6] Cardoso, L. A., Alves Jr, W., Gonzaga, A. R., Aguiar, L. M., and Andrade, H. M. Friedel-Crafts acylation of anisole with acetic anhydride over silica-supported heteropolyphosphotungstic acid (HPW/SiO_2). *Journal of Molecular Catalysis A: Chemical*, 209(1-2):189–197, 2004.

[7] Tiwari, M. S. and Yadav, G. D. Kinetics of Friedel-Crafts benzoylation of veratrole with benzoic anhydride using $Cs_{2.5}H_{0.5}PW_{12}O_{40}$/K-10 solid acid catalyst. *Chemical Engineering Journal*, 266:64–73, 2015.

[8] Gharib, A., Jahangir, M., and Scheeren, J. Acylation of aromatic compounds by acid anhydrides using Preyssler's anion [NaPWO] and heteropolyacids as green catalysts. *Polish Journal of Chemical Technology*, 13(2):11–17, 2011.

[9] Yang, X., Yasukawa, T., Yamashita, Y., and Kobayashi, S. Development of trifluoromethanesulfonic acid-immobilized nitrogen-doped carbon-incarcerated niobia nanoparticle catalysts for Friedel-Crafts acylation. *The Journal of Organic Chemistry*, 86(21):15800–15806, 2021.

[10] Nguyen, M. T. T., Le, N., Nguyen, H. T., Luong, T. D. V., Nguyen, V. K. T., Kawazoe, Y., Tran, P. H., and Pham-Tran, N. N. Mechanism of Friedel–Crafts

acylation using metal triflate in deep eutectic solvents: An experimental and computational study. *ACS Omega*, 8(1):271–278, 2022.

[11] Ji, P., Feng, X., Oliveres, P., Li, Z., Murakami, A., Wang, C., and Lin, W. Strongly lewis acidic metal–organic frameworks for continuous flow catalysis. *Journal of the American Chemical Society*, 141(37):14878–14888, 2019.

[12] Koujout, S. and Brown, D. R. The influence of solvent on the acidity and activity of supported sulfonic acid catalysts. *Catalysis Letters*, 98:195–202, 2004.

[13] Tran, P. H., Nguyen, H. T., Hansen, P. E., and Le, T. N. Greener Friedel-Crafts acylation using microwave-enhanced reactivity of bismuth triflate in the Friedel-Crafts benzoylation of aromatic compounds with benzoic anhydride. *ChemistrySelect*, 2(1):571–575, 2017.

[14] Yang, X., Yasukawa, T., Maki, T., Yamashita, Y., and Kobayashi, S. Well-dispersed trifluoromethanesulfonic acid-treated metal oxide nanoparticles immobilized on nitrogen-doped carbon as catalysts for Friedel–Crafts acylation. *Chemistry–An Asian Journal*, 16(3):232–236, 2021.

[15] Pla, D. and Gómez, M. Metal and metal oxide nanoparticles: A lever for C–H functionalization. *ACS Catalysis*, 6(6):3537–3552, 2016.

[16] Gadipelly, C. and Mannepalli, L. K. Nano-metal oxides for organic transformations. *Current Opinion in Green and Sustainable Chemistry*, 15:20–26, 2019.

[17] Dhinagaran, G., Harichandran, G., Suvaitha, S. P., and Venkatachalam, K. Catalytic activity of SBA-15 supported CuO for selective oxidation of veratryl alcohol to veratraldehyde. *Molecular Catalysis*, 528:112454, 2022.

[18] Mureddu, M., Ferino, I., Musinu, A., Ardu, A., Rombi, E., Cutrufello, M. G., Deiana, P., Fantauzzi, M., and Cannas, C. MeO_x/SBA-15 (Me= Zn, Fe): Highly efficient nanosorbents for mid-temperature H_2S removal. *Journal of Materials Chemistry A*, 2(45):19396–19406, 2014.

[19] Malhotra, R. and Ali, A. 5-Na/ZnO doped mesoporous silica as reusable solid catalyst for biodiesel production via transesterification of virgin cottonseed oil. *Renewable Energy*, 133:606–619, 2019.

[20] Samadi, S., Ashouri, A., and Ghambarian, M. Use of CuO encapsulated in mesoporous silica SBA-15 as a recycled catalyst for allylic C–H bond oxidation of cyclic olefins at room temperature. *RSC Advances*, 7(31):19330–19337, 2017.

[21] Chytil, S., Haugland, L., and Blekkan, E. A. On the mechanical stability of mesoporous silica SBA-15. *Microporous and Mesoporous Materials*, 111(1-3):134–142, 2008.

[22] Dhinagaran, G., Prashanna Suvaitha, S., Muthukumaran, M., and Venkatachalam, K. Chemoselective catalytic oxidation of olefin derivatives with Co–salen immobilized SBA-15. *Catalysis Letters*, 151:1361–1375, 2021.

[23] Sakeye, M. and Smatt, J. H. Comparison of different amino-functionalization procedures on a selection of metal oxide microparticles: degree of modification and hydrolytic stability. *Langmuir*, 28(49):16941–16950, 2012.

[24] Su, D., Xie, X., Munroe, P., Dou, S., and Wang, G. Mesoporous hexagonal Co_3O_4 for high performance lithium ion batteries. *Scientific Reports*, 4(1):6519, 2014.

[25] Tammina, S. K., Mandal, B. K., Ranjan, S., and Dasgupta, N. Cytotoxicity study of *Piper nigrum* seed mediated synthesized SnO_2 nanoparticles towards colorectal (HCT116) and lung cancer (A549) cell lines. *Journal of Photochemistry and Photobiology B: Biology*, 166:158–168, 2017.

[26] Bhuyan, D., Saikia, M., and Saikia, L. ZnO nanoparticles embedded in SBA-15 as an efficient heterogeneous catalyst for the synthesis of dihydropyrimidinones via Biginelli condensation reaction. *Microporous and Mesoporous Materials*, 256:39–48, 2018.

[27] Yang, Z., Yang, Y., Zhu, X., Chen, G., and Zhang, W. An outward coating route to CuO/MnO_2 nanorod array films and their efficient catalytic oxidation of acid fuchsin dye. *Industrial & Engineering Chemistry Research*, 53(23):9608–9615, 2014.

[28] Liu, X. Y., Li, X. P., Zhao, R. X., and Zhang, H. A facile sol-gel method based on urea-$SnCl_2$ deep eutectic solvents for the synthesis of SnO_2/SiO_2 with high oxidation desulfurization activity. *New Journal of Chemistry*, 45(35):15901–15911, 2021.

[29] Yao, Y., Li, Y., Li, C., Zhou, J., Wu, Q., Zheng, Y. Z., Wu, J., Zhou, Z., Ding, H., and Tao, X. Core-shell structured bi-amorphous SiO_2@TiO_2 composite for lithium-ion batteries anode material with ultra-stable performance. *ChemistrySelect*, 5(17):5198–5204, 2020.

[30] Qiu, S., Zhou, H., Shen, Z., Hao, L., Chen, H., and Zhou, X. Synthesis, characterization, and comparison of antibacterial effects and elucidating the

mechanism of ZnO, CuO and CuZnO nanoparticles supported on mesoporous silica SBA-3. *RSC Advances*, 10(5):2767–2785, 2020.

[31] Mahjoub, M. A., Monier, G., Robert-Goumet, C., Réveret, F., Echabaane, M., Chaudanson, D., Petit, M., Bideux, L., and Gruzza, B. Synthesis and study of stable and size-controlled ZnO–SiO_2 quantum dots: Application as a humidity sensor. *The Journal of Physical Chemistry C*, 120(21):11652–11662, 2016.

[32] Zou, Y., Zhou, X., Xie, J., Liao, Q., Huang, B., and Yang, J. A corn-like graphene-SnO_2-carbon nanofiber composite as a high-performance Li-storage material. *Journal of Materials Chemistry A*, 2(13):4524–4527, 2014.

[33] Tomer, V. K., Duhan, S., Malik, R., Nehra, S. P., and Devi, S. A novel highly sensitive humidity sensor based on ZnO/SBA-15 hybrid nanocomposite. *Journal of the American Ceramic Society*, 98(12):3719–3725, 2015.

[34] Gao, G., Zhao, Q., Yang, C., and Jiang, T. *p*-Toluenesulfonic acid functionalized imidazole ionic liquids encapsulated into bismuth SBA-16 as high-efficiency catalysts for Friedel-Crafts acylation reaction. *Dalton Transactions*, 50(17):5871–5882, 2021.

[35] Morizur, V., Szafranek, J., Bonhomme, D., Olivero, S., Desmurs, J. R., and Du, E. Catalysis of the acylation of aromatic derivatives by metallic tosylates. *Tetrahedron*, 71(38):6813–6817, 2015.

[36] Desai, D. S. and Yadav, G. D. Friedel-crafts acylation of furan using chromium-exchanged dodecatungstophosphoric acid: effect of support, mechanism and kinetic modelling. *Clean Technologies and Environmental Policy*, 23:2429–2441, 2021.